Supplemental Information

Time-Delayed Integration – Spectral Flow Cytometer (TDI-SFC) for Low-Abundance-Cell Immunophenotyping

Wenting Hu,[1,2] Steven A. Soper,[1,2,3,4†] and J. Matt Jackson[1,2,†]

[1]Department of Chemistry, University of Kansas; [2]Center of BioModular Multi-Scale Systems for Precision Medicine (CBM[2]), University of Kansas; [3]Department of Mechanical Engineering, University of Kansas; [4]Department of Cancer Biology, University of Kansas Medical Center

[†]Corresponding authors: ssoper@ku.edu, mattjackson@ku.edu

Table of Contents

Excitation power and non-uniformity in Köhler epi-illumination for 7.1× and 21.2× beam expanders

For excitation, we enlarged a 488 nm laser (54 mW) with a beam expander then used a circular aperture to cut the wings of the Gaussian laser beam to give a more uniform intensity profile within the CCD's field-of-view and eliminate illumination outside the CCD sensor's field-of-view (Köhler epi-illumination). After beam expansion, the beam's radius (w = 1/e^2 = 0.65 mm) was enlarged by a factor of 7.1× or 21.2× to w = 4.6 mm or 13.8 mm, respectively. With either beam expander, the total beam power P_0 = 54 mW remained constant, but as the beam expanded, the laser power density became more uniform (**Fig. S1**). The profile of the enlarged beams is given by a Gaussian function over radius r:

$$I(r) = \frac{2P_0}{\pi w^2} e^{-\frac{2r^2}{w^2}} \qquad \text{(Eq. S1)}$$

Integration of Eq. S1 over the aperture's fixed surface area, $\pi d^2/4$, showed that the total power should increase from 5.7 mW to 40.6 mW when decreasing the beam size using a 21.2× or 7.1× beam expander. These theoretical calculations agreed well with the experimental measurements of 4 mW and 21 mW, respectively. Lastly, we note that while the power density non-uniformity increased to 15% (RSD) with the 7.1× beam expander, even the lowest intensity excitation at the edge of the field-of-view surpassed the power density achieved with a 21.2× beam expander.

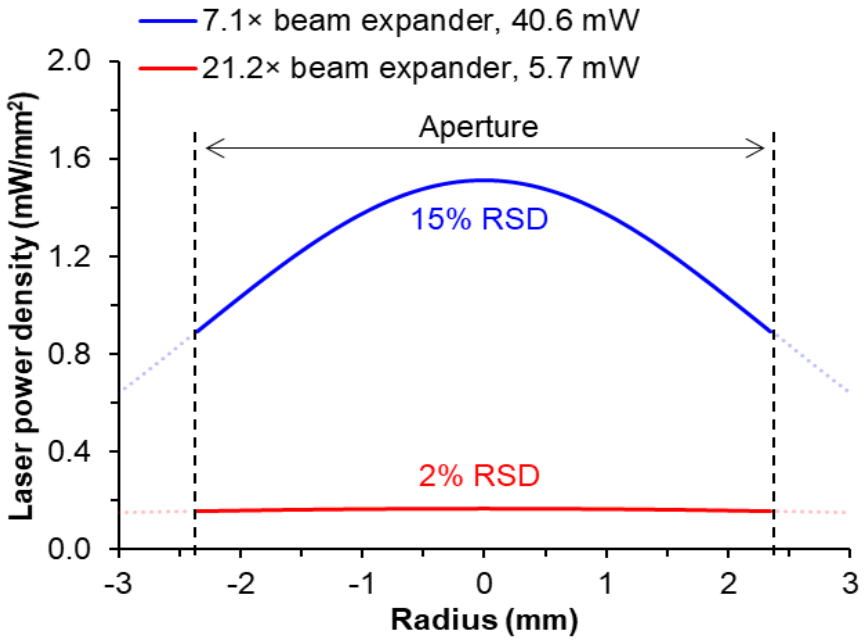

Figure S1. Theoretical power density of the 488 nm excitation laser through the epi-illumination aperture for the 7.1× and 21.2× beam expanders.

Simulations for the effect of TDI synchronization on signal output

A time-stepping simulation in Fortran 90 (provided in full below) was written to progressively move a particle or cell (6 µm) along a CCD column with 100 pixel rows (2 µm/pixel). We set the TDI time delay to 2 ms so a particle, perfectly synchronized with respect to the CCD clocking rate, would be moving at a linear velocity of $2\ \mu m/2\ ms = 1\ mm/s$. We set the particle at an initial position outside of the field-of-view of the collection objective (see **Fig. 1A**) and progressively shifted the particle forward every 0.02 ms with a linear velocity ranging from 0.1-10 mm/s. We added a simulated signal to the underlying pixel grid and independent of the particle's position, we shifted the accumulated signal in each pixel row towards the serial register every 2 ms as stated above. We read the signal from the serial register of the CCD (in arbitrary intensity units) until the particle exited the field-of-view and all signal was read from the CCD (**Fig. 2A**).

At perfect synchronization (1 mm/s particle linear velocity), we observed a minimized event duration and maximized peak signal (**Fig. S2**). A maximized signal corresponded to the particle's signal appearing on the least amount of CCD pixels and being integrated into the least amount of serial register reads. When the particle velocity decreased or increased, the peak signal decreased as the image became slurred on readout. At lower particle velocities, the integrated signal increased as the slurred image resides on the CCD for a longer period, but such an event may become undetectable if the peak signal is not above the CCD's signal-to-noise detection threshold. Based on the data in **Fig. S2B**, we chose the peak signal and event duration to evaluate the effectiveness of TDI synchronization in **Fig. 3** of the main text.

Note that this simulation does not account for entry time of the particle, *i.e.,* whether or not the entry of the particle arrives at the exact moment after a shift of the CCD. In fact, this is not the most likely scenario, and rather than a single read, it is likely that the particle will occupy two or more reads. Yet we note that this error should not affect the trends in event duration or TDI signal observed in **Fig. S2**, and peak signal and event duration remain accurate metrics for TDI synchronization in the main manuscript.

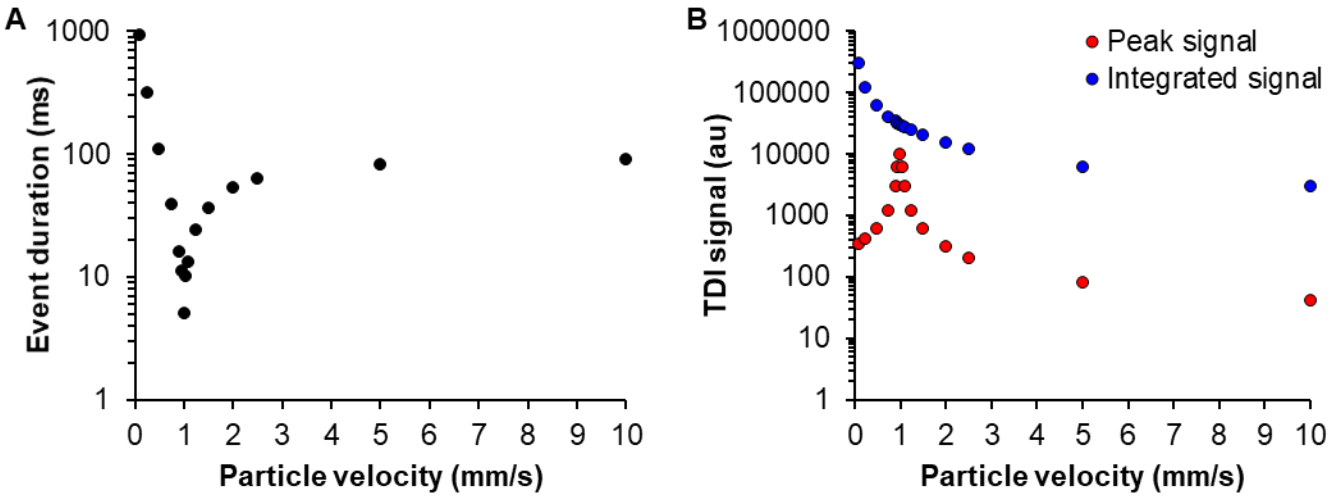

Figure S2. TDI signals when the particle/cell velocity (1 mm/s) was synchronized with the CCD time delay (2 ms) or slightly out of synchronization. Shown is the effect of synchronization between particle/cell and TDI clocking rate on: **(A)** The duration of the event; and **(B)** the peak signal and integrated signal. Note that at velocities lower than 1 mm/s, the peak signal decreases but total integrated signal increases due to higher residence times of the particle/cell within the field-of-view.

Fortran 90 code for TDI simulation

```
program TDISim

implicit none
real :: readtime, pixelsize, beadsize, dt, perfectspeed, speed, beadpos, beadposmin, beadposmax, time, speedratio
logical :: output
integer :: pixelN, j, pixelperbead, t, tout, tmax, intstart, intstop, timestepping
real, dimension(1:100) :: pixelposmin, pixelposmax
real, dimension(:), allocatable :: pixelintensity, signaloutput

speedratio = 1.e0 !synchronization, 1 is perfect
timestepping = 100 !time step for simulation will be readtime/timestepping
readtime = 2.e-3 !Readout time per row, in s
pixelsize = 2.e0 !Size of pixels
beadsize = 6.e0 !Size of particle
pixelN = 100 !Number of rows on CCD

pixelperbead = ceiling(beadsize/pixelsize)
dt = readtime/timestepping
perfectspeed = pixelsize / readtime
beadpos = -beadsize*2.e0
speed = speedratio * perfectspeed
```

```
t = 1
tout = 1
time = 0.e0 !initialize time
output = .false.

tmax = ceiling((pixelN*pixelsize)/speed/(dt*timestepping))*10
allocate(signaloutput(tmax))
allocate(pixelintensity(tmax*timestepping))
signaloutput(1:tmax)=0
pixelintensity(1:tmax*timestepping)=0

do j = 1,pixelN
   pixelposmin(j) = (j-1)*pixelsize
   pixelposmax(j) = (j)*pixelsize
end do

open(unit = 20,file="SignalOutput.txt")
write(20,*) "Relative speed to perfect: ", speedratio

do t = 1,tmax*timestepping
   beadposmin = beadpos - beadsize/2.e0
   beadposmax = beadpos + beadsize/2.e0
   intstart = ceiling(beadposmin/pixelsize)
   intstop = ceiling(beadposmax/pixelsize)

   do j=intstart+1,intstop-1
      if (j>=1 .and. j<=pixelN) then
         pixelintensity(j) = pixelintensity(j) + 1.e0
      end if
   end do

   if (intstart >= 1 .and. intstart <= pixelN) then
      pixelintensity(intstart) = pixelintensity(intstart) + (pixelposmax(intstart)-beadposmin)/pixelsize
   end if

   if (intstop >= 1 .and. intstop <= pixelN) then
      pixelintensity(intstop) = pixelintensity(intstop) + (beadposmax - pixelposmin(intstop))/pixelsize
   end if

   if (mod(t,timestepping) == 0 ) then
      signaloutput(tout) = pixelintensity(pixelN)
      write(20,*) time, signaloutput(tout)

      do j=pixelN,1,-1
         if (j>1)then
            pixelintensity(j)=pixelintensity(j-1)
         else
            pixelintensity(j) = 0.e0
         end if
      end do

      if (signaloutput(tout) > 0) then
         output = .true.
      end if

      if (signaloutput(tout) == 0.e0 .and. output .eqv. .true.) then
         exit
      end if

      tout = tout + 1

   end if

   time = time + dt
   beadpos = beadpos + dt*speed

end do
close(20)
end program
```

Correlation between fluorescence calibration beads and antibody binding capacity (ABC) beads

We compared fluorescent calibration beads used for TDI-SFC optimization, which have an arbitrary intensity ranging from 0.3% to 100%, with ABC beads. ABC beads contain Fc-specific receptors and carry a known, quantitative load of fluorescent antibodies – note that full loading of the ABC beads was ensured by increasing antibody concentration without any increase in fluorescence signal. Both calibration beads and ABC beads were measured by traditional flow cytometry (**Fig. S3**). Only the 0.3% calibration beads were within the dynamic range of the ABC beads ($3.8 \pm 0.2 \times 10^5$ antibodies). However, assuming linearity beyond the ABC populations available, the 1% calibration beads would correspond to a load of $2.2 \pm 0.1 \times 10^6$ antibodies. For a frame of reference, direct immunolabeled surface antigens typically fall in a range of 10^3-10^6 antibodies per biological cell.

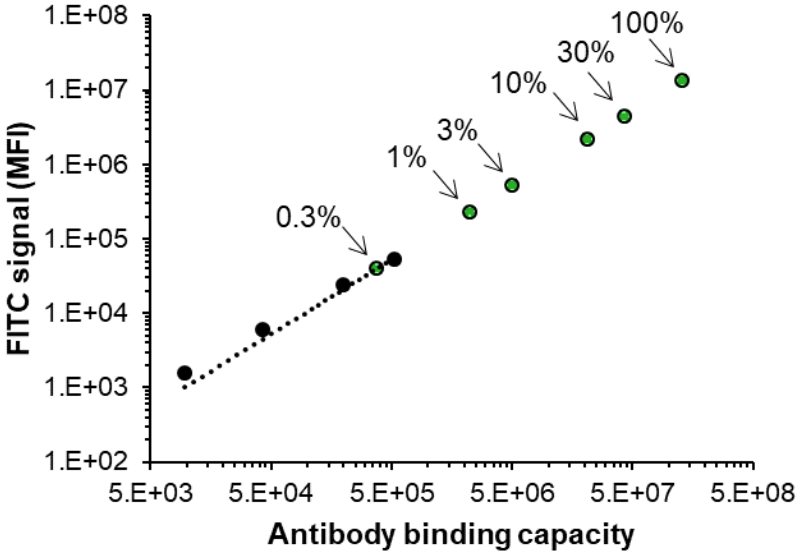

Figure S3. Labeled anti-mouse IgG Fc-specific beads with varying antibody binding capacity with mouse, anti-human TdT-FITC antibodies. Each population of ABC beads was measured using a traditional flow cytometer and the mean fluorescence intensity (MFI) was extracted. Fluorescence from the calibration beads was then measured, and the calibration beads' MFI values were correlated with the ABC values. The linear fit between MFI and ABC values is shown in black (R^2 = 0.995). A linear fit was also obtained between MFI and percent fluorescence for the calibration beads (data not shown, N = 2, R^2 = 0.996). Note that we subtracted all positive populations with the MFI of their respective blank, unlabeled beads.

Signal-to-noise ratio (SNR) calculations for TDI fluorescence spectra

A TDI event consists of a fluorescence spectrum read over time, S(λ,t). To assess the effect of the variables in **Table 1** on fluorescence sensitivity and SNR, we accumulated all signal processed by the CCD by integrating the total signal S_{int} over all wavelengths and over the event's duration Δt. We then evaluated noise in each fluorescence spectrum integrated over time, *i.e.*, $\int_0^{\Delta t} S(\lambda, t)dt$, by fitting a spline function, $F_{fit}(\lambda)$. The residuals from the fitting function represent noise in the integrated spectrum that was quantitated by the sum of square errors (SSE) over all wavelengths. We note that we did not observe a dependence on the SNR (Eq. 3 of the main text) on the wavelength region used to sum the noise. An example of the fitting process is shown in **Fig. S4**, where an increase in shot noise is evident as the fluorescence signal increases.

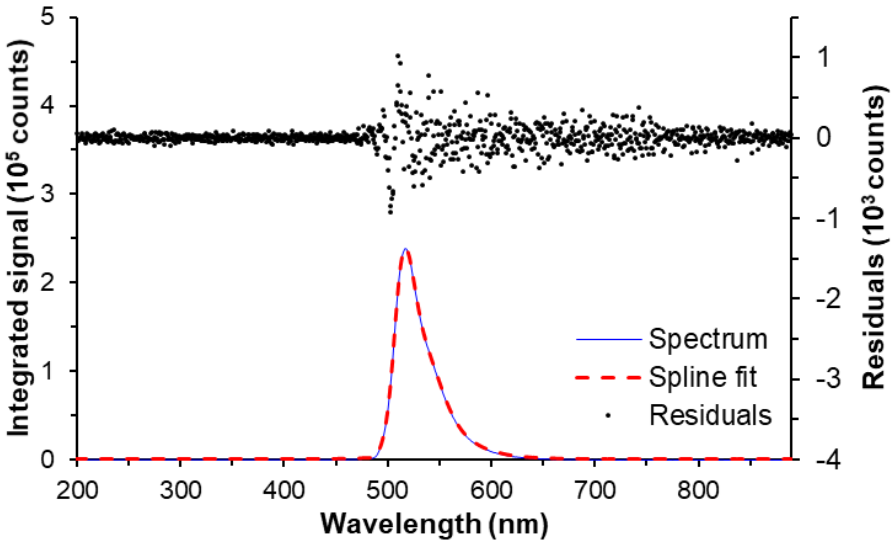

Figure S4. An integrated spectrum was fit with a spline function (smoothing parameter = 0.1). Residuals in the fit represented noise in the integrated signal, quantified by the sum of square errors (SSE).

COMSOL fluid dynamic simulations for the microfluidic flow cell

We evaluated the flow velocity profiles within the microfluidic T-cell with hydrodynamic focusing using 3-D laminar flow simulations in COMSOL Multiphysics 5.2a. We constructed the geometry using measurements of the microchannel cross section obtained from laser scanning profilometry, which we provide along with all other parameters of the simulations in **Table S1**. We evaluated the flow profile in a square bore capillary with no hydrodynamic focusing using the same simulation parameters, except that the geometry was designed as a 1 mm long segment of a 75 µm square channel. We show axial cross sections of the velocity flow profiles in the sheathed sample stream in **Fig. S5** with the maximum velocities and core widths noted. Results for the square capillary are not shown, but these results indicated a maximum velocity of 4.19 mm/s and average velocity of 2 mm/s for the volume flow rate tested, which was 0.675 µL/min. We also note that we observed variation in the maximum wavelength of bead spectra during TDI-SFC imaging, which correlates with the core width of the sheathed sample stream (**Fig. S5C**), because the spatial x-axis is spectrally dispersed into the wavelength axis of the TDI-SFC CCD (see **Fig. 1A**).

Table S1. All simulation parameters for 3-D COMSOL Multiphysics simulations of velocity fields.

Simulation parameter	Value
Geometry lengths	1.5 mm (sample), 1 mm (both sheaths)
Geometry height	92.6 µm
Geometry width (top)	124.6 µm
Geometry width (bottom)	70.6 µm
Fluid properties	Water
Wall conditions	No slip
Inlet condition	0.12 µL/min (sample), 0.12-0.21 µL/min (sheath)
Outlet condition	0 Pa
Initial values	0 velocity field, 0 pressure drop
Meshing preset	Physics-controlled, “Extra fine”
Number of elements	2,823,023
Element size	0.456-7 µm
Maximum element growth rate	1.08
Resolution of curvature	0.3
Resolution of narrow regions	0.95
Number of boundary layers	2
Boundary layer stretching factor	1.2
Thickness adjustment factor	5
Solution type	Stationary
Solver	GMRES, fully coupled (default settings)
Relative tolerance for convergence	10^{-3}

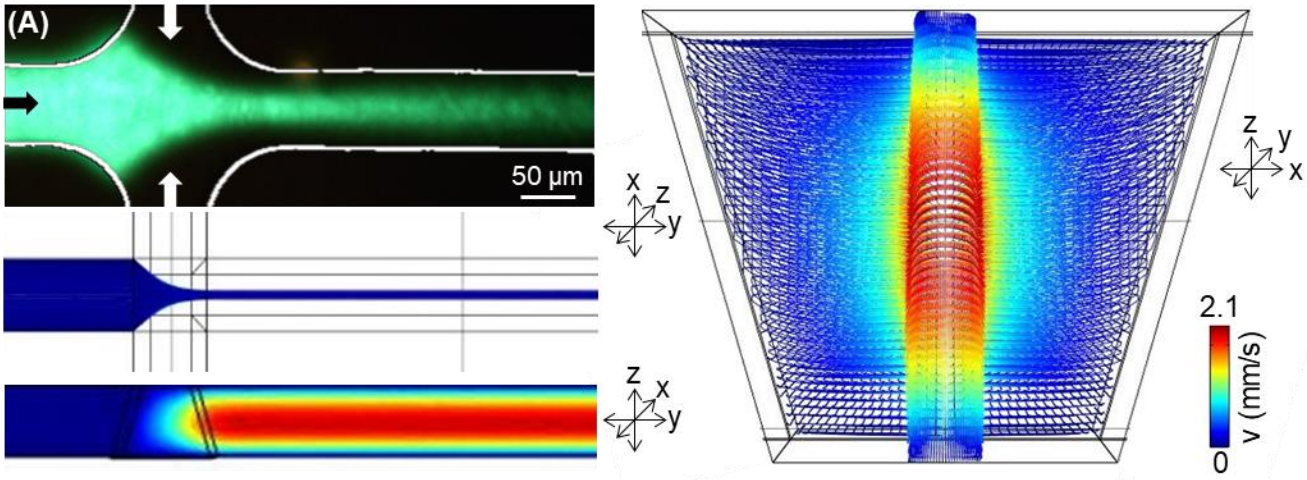

(B)

Sheath rate (µL/min)	Core width (µm)	V_{max} (mm/s)	V_{ave} (mm/s)	RSD
0.120	24.0	1.41	0.91 ±0.41	
0.138	22.0	1.55	1.01 ±0.45	
0.156	20.2	1.69	1.10 ±0.50	45%
0.174	18.6	1.83	1.20 ±0.54	
0.192	17.6	1.97	1.29 ±0.58	
0.210	16.4	2.11	1.39 ±0.62	
None	92.0	0.47	0.24 ±0.16	66%

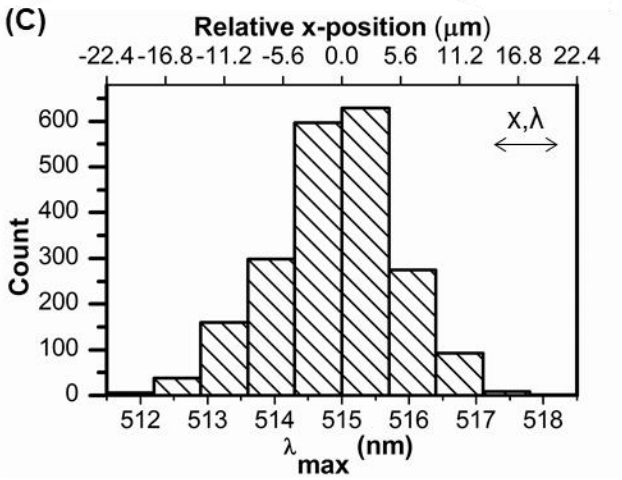

Figure S5. (A) Fluorescence image while focusing FITC dye with a 0.138 µL/min sheathing rate, and 3-D COMSOL simulations results for the microfluidic T-shaped flow cell with hydrodynamic flow focusing showing streamline plots viewed from the top (top-left panel), side (bottom-left panel), and cross-section (right panel) for a sheath flow rate of 0.210 µL/min. **(B)** Table showing the maximum velocity and core width of the sheathed sample stream for the sheathing rates tested in the main text. No sheathing fluid indicates values for the sample channel alone. **(C)** Variation in the peak wavelength for bead spectra (obtained with a sheath rate of 0.174 µL/min) correlates with variation in bead position along the x-direction of the flow cell (core width).

Fluorescence signals for out-of-focus particles/cells

The effective z-axis spread of particle/cell travel in our system was set by the microfluidic T-cell depth, which was 92 µm. To test the amount of fluorescence processed by the TDI-SFC system when in/out of focus, we dispensed fluorescent calibration beads diluted in water onto a glass slide, sealed the slide with a coverslip, and placed the slide within the TDI-SFC system and imaged through the coverslip. We focused on a single bead via the system's CMOS camera (**Fig. 1A**). The bead was displaced out of the focal plane as measured by a micrometer X-Y-Z sample stage and images were recorded of the out-of-focus fluorescence (**Fig. S6**). Changes in the bead's image were apparent after a 30-µm displacement from the focal plane. After a 50-µm displacement, which is beyond the maximum deviation allowed by the 92 µm deep microfluidic focusing channel, the image was further distorted with signal being imaged onto a larger area of the CCD. These data illustrate that while 1-D focusing does not constrain particle position in the z-direction, particles may still be detected by the TDI-SFC system, albeit with higher variation in signal intensity. In addition, variation in the flow velocity along the z-axis (see **Fig. S5A**) will also cause some particles/cells to not be synchronized to the CCD clocking rate.

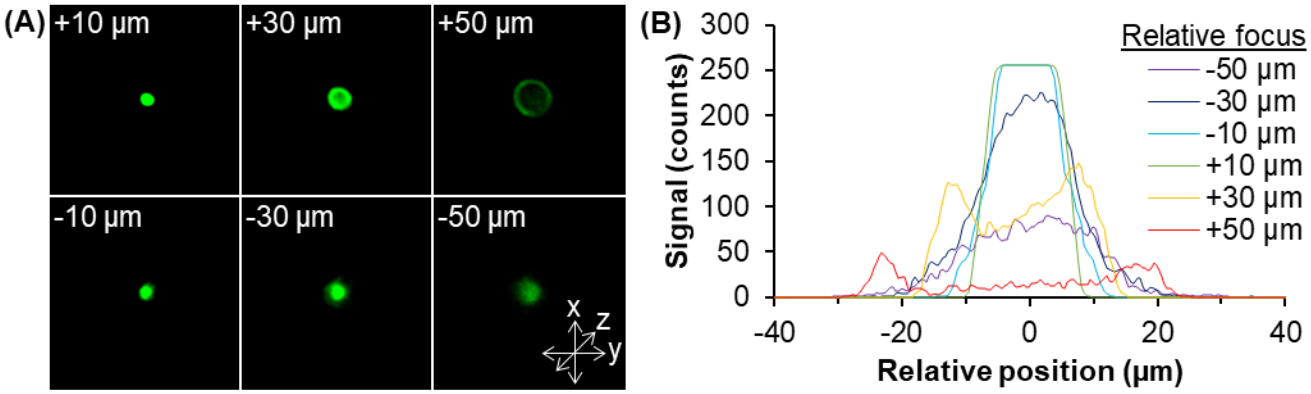

Figure S6. (A) Images from the CMOS focus camera of a single fluorescent bead translated in/out of the TDI-SFC system's focal plane using a micrometer positioning stage. **(B)** Line fluorescence profiles across the bead showing that the bead when shifted out of the system's focal plane generates out-of-focus fluorescence that may still be detected by the TDI-SFC system.

Representative TDI peaks acquired with increased integration times or objective numerical aperture

TDI events representative of the data in **Fig. 3B** are shown in **Fig. S7**. As a note, we included only data that surpassed a threshold of 20× the signal-to-background noise. We also removed all background data between events so we could show several events on the same plot.

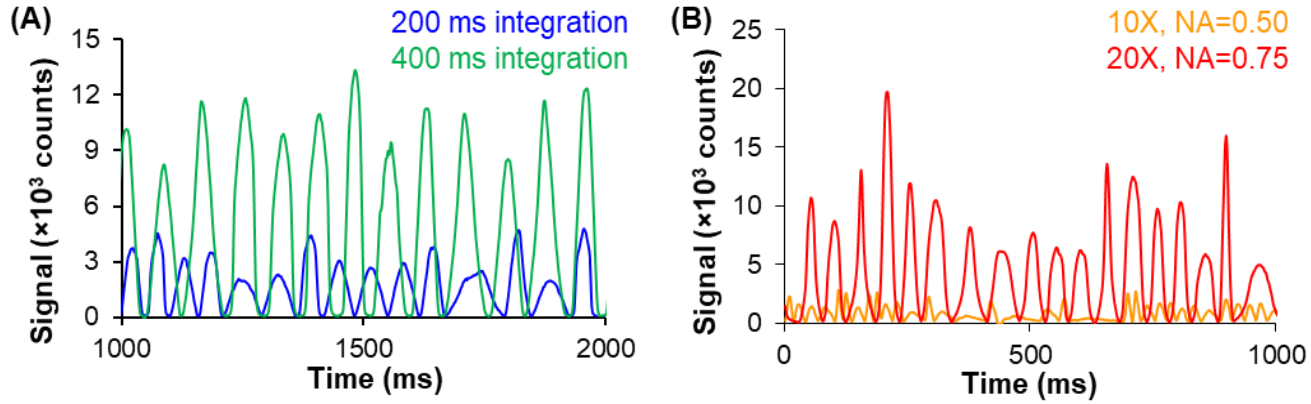

Figure S7. TDI signals at 515 nm for the fluorescent calibration beads. **(A)** Data integrated for 200 ms (2.0 mm/s) or 400 ms (1.20 mm/s) using 100% intensity calibration beads and a 10X objective. **(B)** Data from 1% intensity calibration beads, integrated for 200 ms using a 10X objective (NA=0.50, 1.83 mm/s) or a 20X objective (NA=0.75, 0.92 mm/s). Statistical analysis is provided in **Fig. 3**.

Probability of multiple bead occupancy in the TDI-SFC field-of-view

We processed increasing concentrations of beads through the TDI-SFC system and found an upper limit (750 beads/µL) above which coincident events could not be resolved in time (**Fig. 6**). To determine the probability of occupancy in the TDI-SFC field-of-view, we calculated the detection volume (673 pL) using the sheathed sample width (18.6 µm, **Fig. S5**) and assumed that beads can be detected throughout the microchannel's depth (92 µm) and the CCD's field-of-view (393 µm). We calculated the probability that k beads would occupy the field-of-view simultaneously (**Fig. S8**) assuming a Poisson distribution ($P(k) = e^{-\lambda}\lambda^k/k!$, where λ is the average occupancy (bead concentration multiplied by the detection volume).

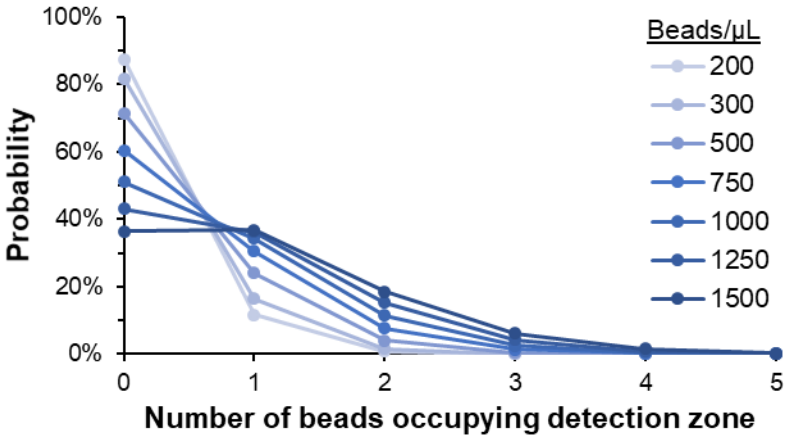

Beads/µL	Probability of multiple occupancy
200	0.8%
300	1.8%
500	4.5%
750	9.2%
1000	14.6%
1250	20.6%
1500	26.7%

Figure S8. Distributions showing multiple bead occupancy over bead concentrations relevant to **Fig. 6**.

Coefficient of variation for bead fluorescence intensity by commercial MFC and TDI-SFC

The 3% intensity beads were evaluated using a commercial MFC and by TDI-SFC, and the measured signal was calculated as the mean fluorescence intensity (MFI) or S_{int} (**Fig. S9**). Commercial MFC yielded an intensity distribution with an MFI of 5.4×10^5 counts with a 6.1% coefficient of variation (CV = MFI/standard deviation). Integrated TDI signals were non-Gaussian and skewed because slower beads reside within the field-of-view longer and generate increased S_{int} even though S_{peak} decreases (**Fig. S2B**). As such, the non-Gaussian distribution makes the normal CV calculation inappropriate. We therefore calculated the CV based on the median signal divided by the interquartile range (refer to box plot insert in **Fig. S9**). This yielded a median S_{int} of 1.9×10^6 and a reduced CV of 24.2%. Recalculating the MFC CV by this definition produced a negligible increase of 1.3%. The relatively high CV by the TDI-SFC can be attributed to variability in bead position along the z-axis because we used only 1-D microfluidic focusing (see **Fig. S5**).

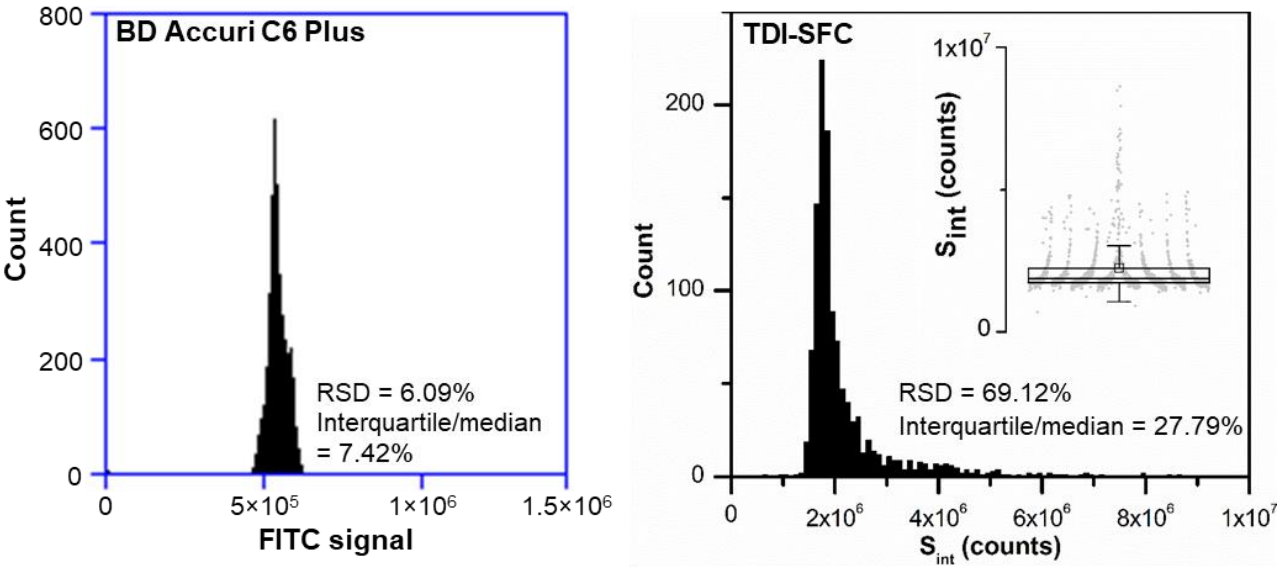

Figure S9. Histograms of fluorescence intensity for 3% intensity beads measured with a commercial MFC and TDI-SFC (10X objective, 200 ms integration). For the TDI-SFC data, a box plot is inlaid to show skew in the signal distribution that led to using the interquartile distance divided by median value for calculating the CV.

Classic least squares unmixing of dye mixtures

We infused mixtures of FITC (1 nM), streptavidin-PE (5 nM), streptavidin-PE-Cy5 (5 nM), and/or streptavidin-PE-Cy7 (50 nM) through a glass capillary. For every possible combination of dyes, results from classic least squares unmixing[1] correctly identified each mixture's composition (**Fig. S10**) without false positives or negatives.

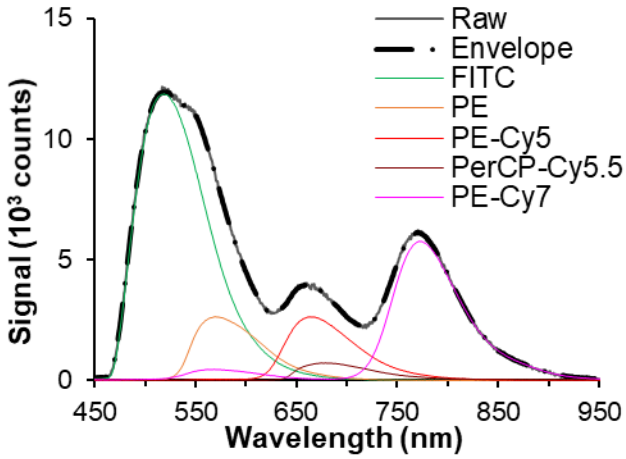

Composition of mixture tested

Dyes detected λ_{em}	FP	F5	F7	FP5	FP7	F57	FP57	P5	P7	P57	57
FITC (F) 518 nm	*F*	*F*	*F*	*F*	*F*	*F*	*F*	-	-	-	-
PE (P) 575 nm	*P*	-	-	*P*	*P*	-	*P*	*P*	*P*	*P*	-
PE-Cy5 (5) 670 nm	-	*5*	-	*5*	-	*5*	*5*	*5*	-	*5*	*5*
PE-Cy7 (7) 767 nm	-	-	*7*	-	*7*	*7*	*7*	-	*7*	*7*	*7*

Figure S10. Mixtures of FITC (F), PE (P), PE-Cy5 (5), and PE-Cy7 (7) were imaged using the TDI-SFC system. Along the columns, mixtures are designated by their components. For example, FP includes FITC and PE but not PE-Cy5 or PE-Cy7, and FP57 includes all components. Resultant spectra were deconvoluted by classic least squares unmixing, and the dyes detected for each mixture are shown along the rows. If a dye was detected in the mixture, the cell was colored and labeled, whereas if the dye was not detected by deconvolution, the cell was shaded grey and marked with a dash.

Autofluorescence in SUP-B15 B-ALL cell line

We observed autofluorescence in a subpopulation of SUP-B15 B-ALL cells that persisted throughout normal culture conditions. In **Fig. S11A**, we show signal in the FITC channel by fluorescence microscopy for a fraction of the SUP-B15 cells that we attributed to autofluorescence with similar autofluorescence appearing in the Cy3 and Cy5 channels (data not shown). To accurately quantitate how many SUP-B15 cells were autofluorescent, we interrogated unstained cells by traditional flow cytometry (**Fig. S11B**). We observed two subpopulations of cells based on the forward scattering (FSC), side scattering (SSC) and FITC channel signals. Approximately half of the cells generated twice as much FSC signal as the other half, concordant with microscopic examinations (**Fig. S11A**). We suspect these cells were actively mitotic and therefore larger.

By examining signal in the FITC channel (**Fig. S11C**), we observed that only a subpopulation of the smaller cells (smaller FSC signal) exhibited increased autofluorescence (~6.4% of all cells in the FSC/SSC gate in **Fig. S11B**). Given the lack of increased autofluorescence in larger cells suspected to be mitotic, we hypothesize that roughly 6% of SUP-B15 cells are apoptotic. We did not test this hypothesis due to interference of autofluorescence with standard annexin V fluorescence staining. However, there is substantial literature precedence for increased autofluorescence at 488 nm during apoptosis, particularly due to oxidation of mitochondrial flavins, such as flavin adenine dinucleotide (FAD).[2]

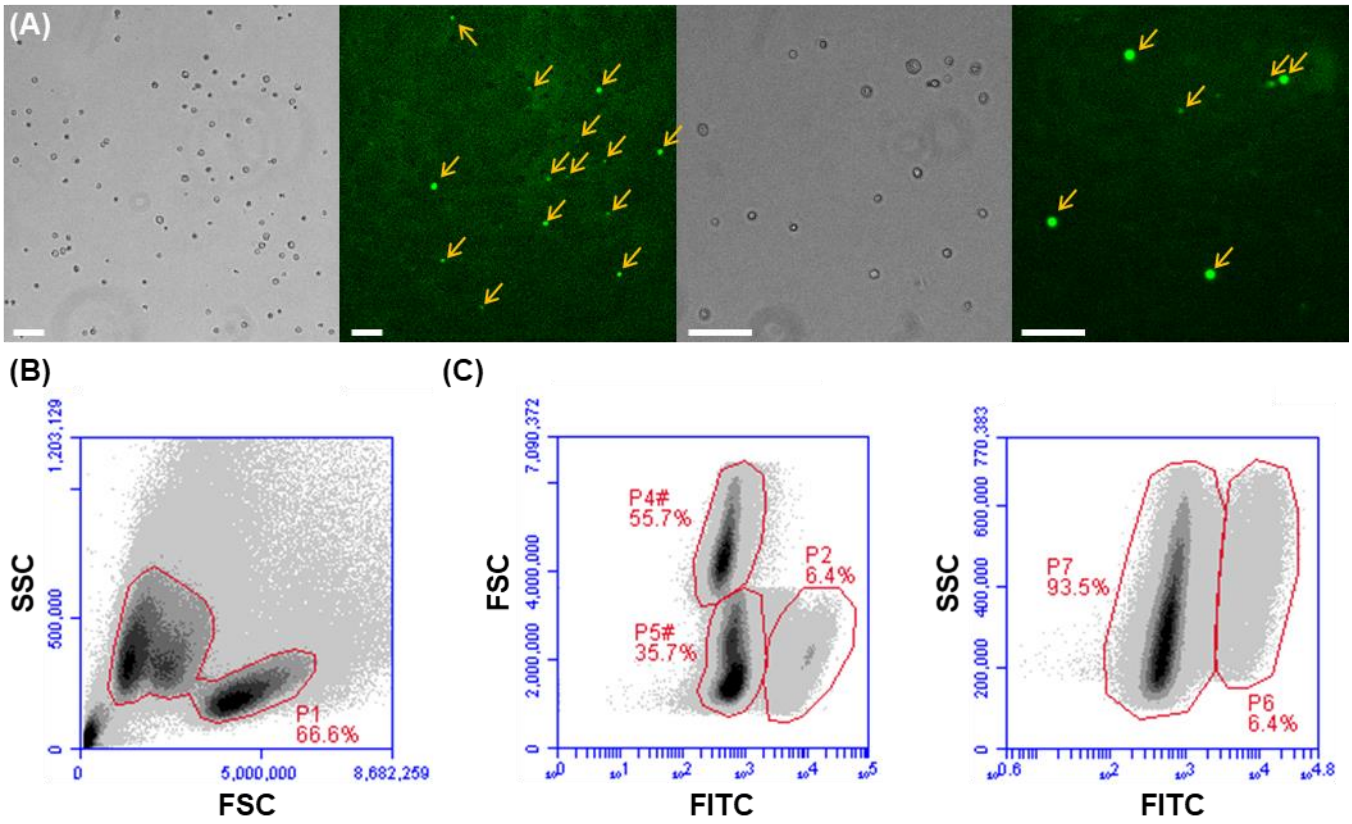

Figure S11. (A) Brightfield (grey) and fluorescence (FITC channel, green) microscopy images of unstained SUP-B15 cells. Yellow arrows mark the presence of cells with increased autofluorescence. All scale bars equal 100 µm. **(B)** Flow cytometry of unstained cells showed two subpopulations of cells with the same SSC signal but differing FSC signal. **(C)** Only the smaller cells (~6.4% of total cells) with lower FSC signal exhibited increased autofluorescence on the FITC channel, whereas we found no correlation between increased FITC signal and SSC. We also note that we observed similar trends on all fluorescence channels (PE, PerCP, APC; data not shown)

Deconvolution of multiplexed fluorescence spectra

We fixed and permeabilized SUP-B15 cells then either left the cells unstained or labeled with 7-AAD, anti-TdT-FITC, or a cocktail of both 7-AAD and anti-TdT-FITC. After processing the cells with the TDI-SFC system, we background subtracted each event and summed signals in all frames throughout a single event duration. These integrated spectra were deconvoluted by curve fitting to determine the contribution of each fluorophore component. Each curve, F(λ), was represented via sums of Gaussian functions:

$$F(\lambda) = \sum_{f=1}^{3} I^f \sum_{i=1}^{N^f} A_i^f \, e^{-\left(\frac{x-\left(\lambda_1^f+\Delta\lambda_i^f\right)}{\sigma_i^f}\right)^2} \qquad \text{Eq. (S2)}$$

In Eq. (S2), I^f is the intensity of a particular fluorophore, f; N^f is the number of Gaussian functions for fluorophore f; and A_i^f is the relative intensity of fluorophore f's i^{th} Gaussian function, which is defined by the standard deviation in wavelength, σ_i^f, and the Gaussian's peak position, $\Delta\lambda_i^f$, that is set relative to the first Gaussian function, λ_1^f.

We used the unstained or singly-stained SUP-B15 cells to determine the curve fitting parameters for autofluorescence and the 7-AAD and FITC fluorophores. We selected the 7-AAD and FITC training sets to be reasonably devoid of autofluorescence components. These spectra agreed well with reference spectra (Thermo Fisher Fluorescence SpectraViewer, **Fig. S12A**).

We note that slight variation in the cells' lateral positions translated to shifting of the fluorescence spectra along the CCD's wavelength axis, generally by 1-5 nm. Thus, each fluorophore's components were not hard set but allowed to slightly shift in position and magnitude according to constraints within a nonlinear, least squares

solver. We outline the curve fitting constraints as well as the median values observed in the training sets in **Table S2** and show the residuals, which were normalized to the maximum signal and averaged over every event in the training set (**Fig. S12B**). Lastly, we note that nonlinear least squares solvers are highly susceptible to poor initial conditions for sums of exponentials. For multiplexed deconvolution, we first used the median values of fitting constraints in **Table S2** to generate an initial condition for a solution using variable fitting constraints.

Table S2. Curve fitting constraints for FITC, 7-AAD, and autofluorescence spectra that were optimized via training sets for a nonlinear, least squares solver.

Component (events)	Variable	Fitting constraints		Median values	
FITC (N=33)	A_1	1.00-1.00		1.00	
	λ_1	512-516	nm	513.7	nm
	σ_1	8-11	nm	9.6	nm
	A_2	1.00-1.00		1.00	
	$\Delta\lambda_2$	11-14	nm	12.2	nm
	σ_2	11-17	nm	14	nm
	A_3	0.57-0.64		0.62	
	$\Delta\lambda_3$	28-35	nm	31.4	nm
	σ_3	21-27	nm	22.9	nm
	A_4	0.18-0.23		0.21	
	$\Delta\lambda_4$	60-66	nm	64	nm
	σ_4	32-38	nm	38	nm
	A_5	0.40-0.48		0.44	
	$\Delta\lambda_5$	-10,-8	nm	-8.9	nm
	σ_5	4-7	nm	5.3	nm
7-AAD (N=165)	A_1	1.00-1.00		1.00	
	λ_1	627-640	nm	628.8	nm
	σ_1	24-34	nm	28.5	nm
	A_2	1.00-1.00		1.00	
	λ_2	25-35	nm	28.6	nm
	σ_2	33-43	nm	32.4	nm
	A_3	0.34-0.40		0.18	
	λ_3	65-71	nm	94	nm
	σ_3	30-36	nm	63	nm
	A_4	0.15-0.21		0.37	
	λ_4	88-94	nm	66.9	nm
	σ_4	57-63	nm	33.2	nm
Autofluorescence (N=22)	A_1	0.30-0.34		0.33	
	λ_1	508-511	nm	508.9	nm
	σ_1	6-8	nm	6.2	nm
	A_2	0.54-0.58		0.57	
	$\Delta\lambda_2$	12-15	nm	13.4	nm
	σ_2	12-15	nm	13.5	nm
	A_3	0.78-0.82		0.64	
	$\Delta\lambda_3$	31-34	nm	97.9	nm
	σ_3	19-23	nm	50.2	nm
	A_4	0.85-0.90		0.27	
	$\Delta\lambda_4$	61-63	nm	146	nm
	σ_4	33-36	nm	77.3	nm
	A_5	0.62-0.66		0.81	
	$\Delta\lambda_5$	96-99	nm	33.7	nm
	σ_5	48-51	nm	22.4	nm
	A_6	0.27-0.31		0.90	
	$\Delta\lambda_6$	142-146	nm	62.4	nm
	σ_6	74-79	nm	34.6	nm

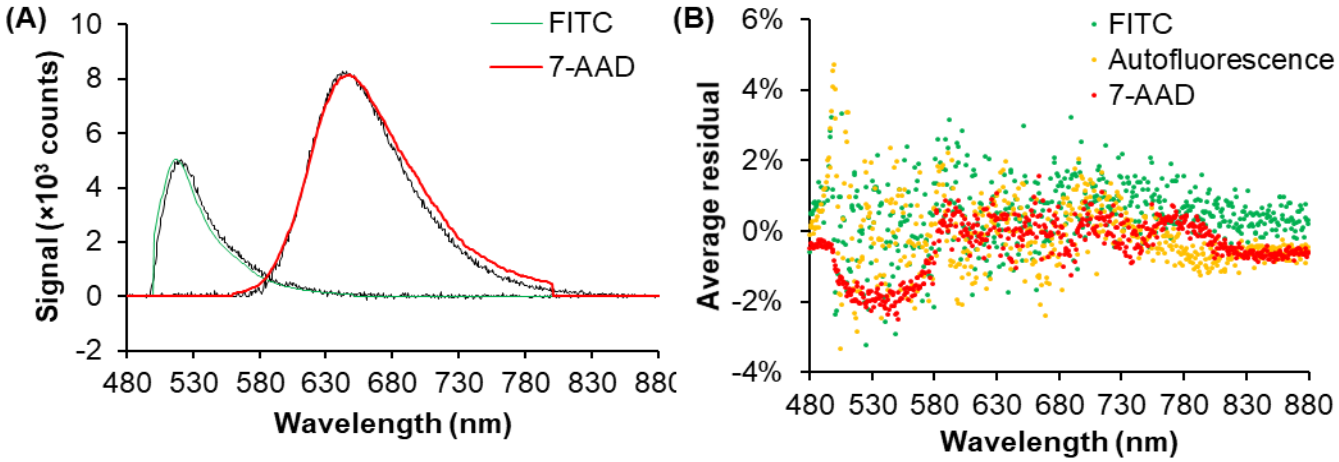

Figure S12. (A) Sample TDI-SFC spectra (black lines) for FITC and 7-AAD compared to reference spectra (colored lines). **(B)** After fitting all curves in the training set using the constraints in **Table S2**, we normalized each spectrum's residuals to peak signals and computed the average residuals over all events.

As shown in **Fig. S11**, ~6% of SUP-B15 cells were autofluorescent. Autofluorescence spectra overlapped significantly with both FITC and 7-AAD spectra (**Fig. 7A**), so we sought to eliminate interfering autofluorescence by deconvolution. We examined the percentage of autofluorescence signal in each event (**Fig. S13**). All unstained cells had little signal attributed to either FITC or 7-AAD by deconvolution, whereas most stained cells had <25% autofluorescence. Thus, in subsequent analysis we excluded cells with ≥25% autofluorescence signal.

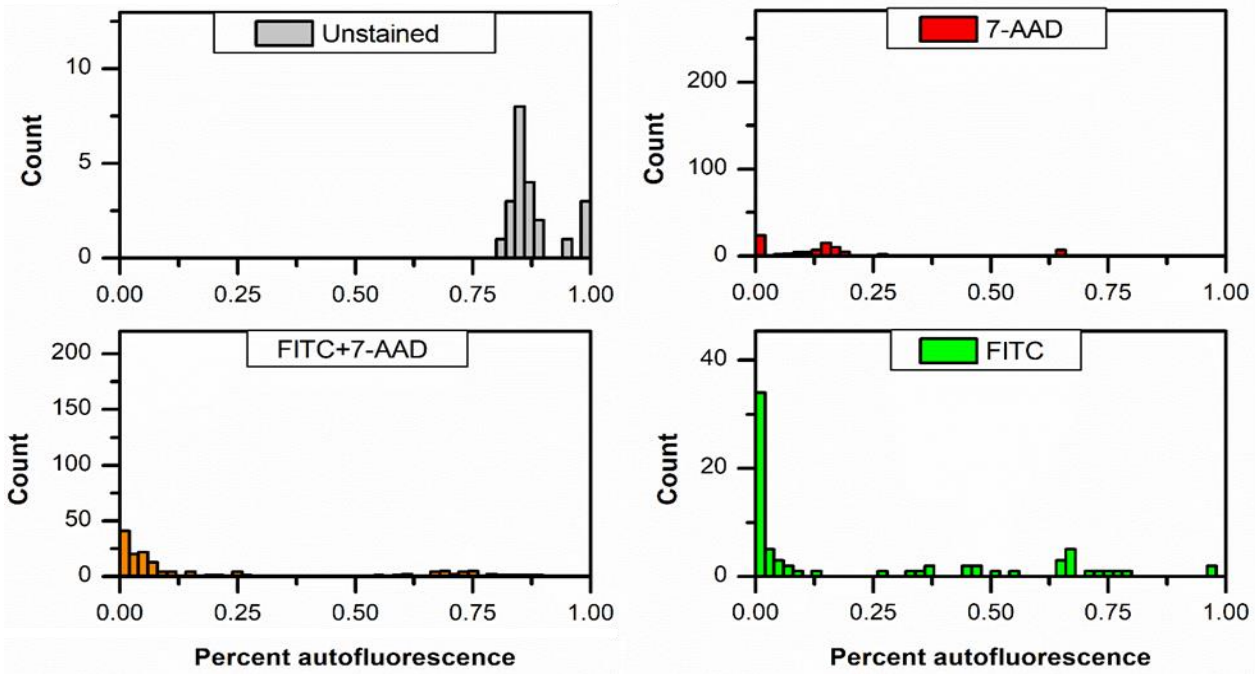

Figure S13. Percentage of signal originating from autofluorescence by multiplexed spectral deconvolution. In all subsequent analyses, cells with ≥25% autofluorescence were excluded.

References

(1) Nolan, J. P.; Condello, D. *Curr Protoc Cytom* **2013**, *Chapter 1*, Unit1 27.
(2) Surre, J.; Saint-Ruf, C.; Collin, V.; Orenga, S.; Ramjeet, M.; Matic, I. *Sci Rep* **2018**, *8*, 12088.